The submitted manuscript has been authored by a contractor of the U.S. Government under Contract No. DE-AC05-00OR22725. Accordingly, the U.S. Government retains a nonexclusive royalty-free license to publish or reproduce the published form of this contribution, or allow others to do so, for U.S. Government purposes.

Sheared flow amplification by vacuum magnetic islands in stellarator plasmas*

L. Garcia
Universidad Carlos III, 28911 Leganés, Madrid, SPAIN

B. A. Carreras, V. E. Lynch
Oak Ridge National Laboratory, Oak Ridge, Tennessee 37831-8070, U.S.A.

M. A. Pedrosa, C. Hidalgo
Asociación EURATOM-CIEMAT, 28040 Madrid, SPAIN

Abstract

There is some experimental evidence that the E×B flows have radial structure that may be linked to rational surfaces. This flow structure may result from a self-organization process involving nonlinear flow amplification through Reynolds stress and fluctuation reduction by sheared flows. In stellarators, a large contribution to the Reynolds stress comes from the coupling of the magnetic field component of a vacuum field island with a plasma instability. In this process, the self-organization principle seems to be marginal stability for the fluctuations driving the flow.

PACs: 52.55.Hc, 52.65.Kj, 52.35.Ra

---

* Research sponsored by the Office of Fusion Energy, U.S. Department of Energy, under contract DE-AC05-00OR22725 with UT-Battelle, LLC and Coop. Agreement DE-FC02-99ER54512.

I. INTRODUCTION

Transport barriers[1,2] in toroidal magnetically confined plasmas tend to be linked to regions of unique magnetic topology, such as the location of a minimum in the safety factor, rational q surfaces, or the boundary between closed and open flux surfaces.[3,4] Recent experimental results have shown the possible influence of low-mode-number islands in the formation of edge transport barriers.[5] In the absence of E×B sheared flows, turbulence is radially nonuniform and has localized structures near resonant surfaces. For pressure-gradient-driven turbulence, fluctuations show maximum amplitude near the rational surface. This localization of the fluctuations might cause the deterioration of confinement in these radial locations, as suggested by the correlation between energy confinement and the presence of low-order rational surfaces at the plasma boundary in Wendelstein 7-AS.[6] On the other hand, if the generation of E×B sheared flows is linked to low order rational surfaces, they cause a local improvement of transport. Measurements of the plasma potential and ion saturation current[7,8] in the boundary region of the TJ-II stellarator[9] have provided experimental evidence for such a link. Therefore, net transport is the result from a self-organization process involving these two mechanisms.

In TJ-II, radial profiles and fluctuations of the ion saturation current have been measured in the proximity of the $n = 8/m = 5$ and $n = 4/m = 2$ natural plasma resonant surfaces. These magnetic surfaces are located near the plasma boundary for different magnetic configurations. The presence of vacuum magnetic field islands at the natural 8/5 and 4/2 rational surfaces has been detected as a flattening in the edge profiles in the plasma configuration. Changes in the shear of E×B flows have been observed near these rational surfaces with values of the shear decorrelation rate $B^{-1}\, dE_r/dr \approx 10^5\ \mathrm{s}^{-1}$. Radial electric fields in the range of 10^3 V/m and poloidal phase velocity of fluctuations of about 500 m/s have been measured.

In this paper, we present a theoretical study of the influence of vacuum magnetic islands on the shear flow amplification near low-resonant surfaces. The nonlinear interaction of the vacuum magnetic islands with plasma turbulence via Reynolds stress is the main mechanism for this flow amplification. Since most of the observations indicate that the effect is important at the plasma edge, we use the resistive interchange model as the most likely instability at the edge of the stellarator.

The way we set up this problem involves single helicity calculations. In the present model, there is no background turbulence. Therefore, this problem involves a reorganization of the

radial profiles of flow and fluctuation and it does not necessarily imply fluctuation suppression by shear flow. Fluctuations and flows organize themselves so as to be close to marginal stability. The vacuum magnetic field perturbation acts as an external knob that allows us to vary this solution and test the nature of this self-organization process.

The rest of the paper is organized as follows. In Sec. II, we present the basic model used to evaluate the nonlinear evolution of the resistive interchange modes. A description of the nonlinear evolution of these instabilities in the presence of vacuum magnetic islands is given in Sec. III. In Sec. IV, we describe the effect of the vacuum magnetic field perturbation on the flow amplification. The self-organization of fluctuations and flow profiles is explained in Sec. V. The presence of a static magnetic field perturbation creates difficulties in the experimental evaluation of statistical properties of fluctuations and flows. These potential difficulties are discussed in Sec. VI. Finally, the conclusions of this paper are given in Sec. VII.

II. NONLINEAR EVOLUTION OF INTERCHANGE MODES

Interchange modes, resistive and ideal, extend uniformly along the magnetic field lines. They are flute-like instabilities. Therefore, it is possible for these instabilities to average over the toroidal magnetic field modulation induced by the helical windings. Using the Greene and Johnson formalism[10] and assuming a straight helical system, the averaged equilibrium magnetic field geometry has cylindrical symmetry. In this system, the magnetic field line curvature is given by the averaged magnetic field line curvature,

$$\kappa \equiv \frac{d\Omega}{dr} = \frac{r}{R_0} B_0^2 V'' \tag{1}$$

where prime indicates the derivative with respect to the toroidal flux, and $V' = \int d\ell / B$ is the specific volume enclosed by a flux surface. In Eq. (1), R_0 is the major radius of the stellarator, r is the averaged minor radius of a flux surface, and B_0 is the toroidal magnetic field value at the magnetic axis.

We use a reduced set of magnetohydrodynamic (MHD) equations to describe the dynamics of the ideal and resistive interchange instability. The geometry is cylindrical with minor radius a and length $L_0 = 2\pi R_0$, and the cylindrical coordinates are r, θ, and z. The reduced set of MHD equations is the poloidal magnetic flux evolution equation:

$$\frac{1}{R_0}\frac{\partial\tilde{\psi}}{\partial t} = -\nabla_{\parallel}\tilde{\Phi} - \frac{1}{|e|n_{eq}}\left(T_{eq}\nabla_{\parallel}\tilde{n} + n_{eq}\nabla_{\parallel}\tilde{T}_e\right) + \eta\tilde{J}_z \quad , \tag{2}$$

and the perpendicular momentum balance equation:

$$\rho_m\frac{\partial\tilde{U}}{\partial t} = -\rho_m\mathbf{v}\cdot\nabla U - B_0\nabla_{\parallel}\tilde{J}_z + \kappa\left(\frac{T_{eq}}{n_{eq}}\frac{1}{r}\frac{\partial\tilde{n}}{\partial\theta} + \frac{1}{r}\frac{\partial\tilde{T}_e}{\partial\theta}\right) + \rho_m\mu\nabla^2\tilde{U} \quad . \tag{3}$$

Since we are applying this model to an electron cyclotron heated stellarator, we assume that the ion temperature is low. Therefore, plasma pressure is essentially given by the electron pressure, $p = p_e \equiv n_e T_e$. We now need an evolution equation for both the electron density and temperature. The electron density equation is

$$\frac{\partial\tilde{n}}{\partial t} = -\mathbf{v}\cdot\nabla n + \frac{1}{|e|}\nabla_{\parallel}\tilde{J}_{\zeta} + D\nabla^2\tilde{n} \quad . \tag{4}$$

The electron temperature equation is

$$\frac{\partial\tilde{T}_e}{\partial t} = -\mathbf{v}\cdot\nabla T_e + \frac{T_{eq}}{|e|n_{eq}}\nabla_{\parallel}\tilde{J}_z + \nabla_{\parallel}\left(\chi_{\parallel}\nabla_{\parallel}T_e\right) + \chi\nabla^2\tilde{T}_e \quad . \tag{5}$$

Here, $\mathbf{v}$ is the perpendicular flow velocity, U is the z-component of the vorticity, ψ is the poloidal magnetic flux function, $J_z = \nabla^2\psi/\mu_0 R_0$ is the parallel current, η is the resistivity, and ρ_m is the mass density. The total magnetic field can be expressed in terms of the poloidal flux function as

$$\mathbf{B} = -\left(\nabla\psi\times\hat{\mathbf{z}}\right)/R_0 + B_0\hat{\mathbf{z}} \quad , \tag{6}$$

and the perpendicular flow velocity in terms of a stream function Φ/B_0 can be expressed as

$$\mathbf{v} = \left(\Phi \times \hat{\mathbf{z}} \right) / B_0 \quad . \tag{7}$$

Here, $\hat{\mathbf{z}}$ is the unit vector in the toroidal direction. The velocity stream function Φ/B_0 is trivially related to the electrostatic potential $-\Phi$. The z-component of the vorticity can be expressed in terms of the velocity stream function by $\tilde{U} = \ ^2 \tilde{\Phi} / B_0$. The derivative parallel to the magnetic field, $_{\|}$, is defined as $_{\|} f = \mathbf{B} \quad f / B_0$.

In Eqs. (2), (3), (4) and (5), a tilde identifies perturbed quantities, and the subindex *eq* identifies equilibrium quantities. The equilibrium current J_{zeq} is assumed to be zero. Each equation has a perpendicular dissipation term with coefficients D , the collisional cross-field particle transport; χ , the perpendicular electron heat conductivity; and μ , the collisional viscosity for the perpendicular flow. The parallel electron heat conductivity, $\chi_{\|}$, is also included in the electron temperature equation.

The driving term of the resistive interchange instability is the pressure gradient in the bad curvature region ($\kappa > 0$). That is, these modes are unstable when $-\kappa \left(dp_{eq} / dr \right) > 0$. The second term on the right-hand-side of Eq. (3) is the field line bending term, which is stabilizing. The resistivity weakens this term and allows the instability to grow.

In the nonlinear calculations, we also include the evolution of the averaged electron density and temperature. The corresponding equations are

$$\frac{\partial \langle n \rangle}{\partial t} = -\frac{1}{r} \frac{\partial}{\partial r} \left(r \Gamma \right) + D_0 \ \frac{1}{r} \frac{\partial}{\partial r} \left(r \frac{\partial \langle n \rangle}{\partial r} \right) \tag{8}$$

and

$$n_{eq} \frac{\partial \langle T_e \rangle}{\partial t} = -\frac{1}{r} \frac{\partial}{\partial r} \left(r \Gamma_Q \right) + \chi_0 \ n_{eq} \frac{1}{r} \frac{\partial}{\partial r} \left(r \frac{\partial \langle T_e \rangle}{\partial r} \right) \quad , \tag{9}$$

where the expressions for the particle and heat flux are

$$\Gamma = \left\langle \tilde{V}_r \tilde{n} \right\rangle - \frac{1}{|e| B_0} \left\langle \tilde{B}_r \tilde{J}_z \right\rangle \tag{10}$$

and

$$\Gamma_Q = n_{eq}\left\langle \tilde{V}_r \tilde{T}_e \right\rangle - \frac{T_{eq}}{|e|B_0}\left\langle \tilde{B}_r \tilde{J}_z \right\rangle - \frac{n_{eq}}{B_0}\left\langle \tilde{B}_r \chi_{\parallel} \quad {}_{\parallel}\tilde{T}_e \right\rangle \quad , \tag{11}$$

respectively. Here, the angular brackets, $\langle\ \rangle$, indicate poloidal and toroidal angle average. The radial derivatives of the equilibrium electron density and temperature in the first term of the right hand side of Eq. (11) are neglected.

The poloidal flow profile evolution equation is derived by taking the flux surface average of the poloidal momentum balance equation. The resulting equation gives the conservation of momentum:

$$\frac{\partial \langle V_\theta \rangle}{\partial t} = -\frac{1}{r^2}\frac{\partial}{\partial r}\left(r^2 S_{r\theta}\right) - \hat{\mu}\langle V_\theta \rangle \quad , \tag{12}$$

where $S_{r\theta}$ is the non-diagonal $r\theta$ component of the Reynolds stress tensor and has two terms, an electrostatic and a magnetic component,

$$S_{r\theta} \equiv \left\langle \tilde{V}_r \tilde{V}_\theta \right\rangle - \frac{1}{\rho_m \mu_0}\left\langle \tilde{B}_r \tilde{B}_\theta \right\rangle \quad , \tag{13}$$

and $\hat{\mu}$ is the poloidal flow damping rate.

The complete set of equations used in the numerical calculations discussed here is Eqs. (2)-(5). Equations (8)-(9) are obtained by flux-surface averaging of Eqs. (4)-(5). Note that the dissipation terms in the averaged equation are not necessarily the same as for the fluctuating quantities. The reason is that the dissipation terms in the fluctuation quantities are used to control the spectrum of Fourier components of the fluctuations, and the ones in the averaged equation correspond to the collisional plasma edge of the TJ-II device. Equation (12) is obtained by flux-surface average of the poloidal momentum balance equation. The dissipative term is a drag instead of a diffusion and is due to magnetic pumping.

We calculate the averaged helical curvature using an equilibrium with the same rotational transform as the TJ-II. The calculations presented here are single helicity 8/5 calculations. We have included 10 poloidal components, from $m = 5$ to $m = 50$, and the radial resolution is $\Delta r/a = 3.3 \times 10^{-3}$.

Nonlinear calculations have been carried out for an equilibrium corresponding to the profiles shown in Fig. 1. The Lunquist number, $S \equiv \tau_R/\tau_{HP}$, is 2.1×10^5; $\beta_0/2\varepsilon^2 = 1.875\times10^{-2}$;

and the diamagnetic frequency, $\omega_{*e} = T_{eq}(0)/|e|a^2 B_0$, is $9.25\times10^{-4}\tau_{Hp}^{-1}$. Here, $\tau_R \equiv a^2\mu_0/\eta(0)$ is the resistive time and $\tau_{HP} \equiv R_0\sqrt{\mu_0\rho_m/B_0}$ is the poloidal Alfvén time. We have used diffusivity coefficients for the fluctuating quantities: $D = \chi = \mu = 0.1a^2/\tau_R$. They are chosen to control the spectrum of modes used in the calculation. For the averaged density and temperature evolution, $D_0 = \chi_0 = 0.3a^2/\tau_R$. The collisional flow damping rate, $\hat{\mu}$, is $200\tau_R^{-1}$, and the parallel electron heat conductivity is $\chi_{||} = 10^5 R_0^2/\tau_R$.

III. DYNAMICS OF RESISTIVE INTERCHANGE INSTABILITIES IN THE PRESENCE OF A VACUUM MAGNETIC ISLAND

A possible explanation of the flow structure near a singular surface is the coupling of the vacuum-magnetic-field island with a plasma instability. Of course, the self-interaction of a vacuum magnetic field perturbation gives an identically zero contribution to the Reynolds stress. It is only the cross-interaction with resonant plasma instabilities that may give a non-zero contribution. Therefore, we will study first the dynamics of the resistive interchange instabilities in the presence of a vacuum magnetic island.

To study the effect of the vacuum magnetic field perturbation on flow amplification, we use the cylindrical-geometry resistive interchange model described in the previous section. To determine the equilibrium parameters, we use the rotational transform profile determined from vacuum magnetic field calculations for a configuration like the TJ-II stellarator (Fig. 1). The vacuum magnetic field island is introduced through a non-zero boundary condition for the $n = 8/m = 5$ component of the poloidal flux. The reference plasma parameters are close to those of TJ-II. In Fig. 1, we have plotted the electron density and temperature profiles, normalized to their peak values, that we have used in the calculations. Since the plasma edge is collisional, we have taken the flow damping rate to be equal to the ion-ion collision frequency, ν_i, and we assumed $T_i = T_e = 20$ eV. The present calculations are not a simulation of the TJ-II results. The magnetic geometry of the TJ-II stellarator is not amenable to the averaging method treatment. Here, we use TJ-II parameters only as a reference for these calculations.

We control the size of the 5/8 vacuum magnetic field island by varying the boundary condition for the ($m = 5$; $n = 8$) component of the poloidal magnetic flux, ψ_b. In the

nonlinear calculations, we vary ψ_b from $\psi_b = 0$ to $\psi_b = 5\times10^{-4}$; the corresponding vacuum magnetic island width changes from $W = 0$ to $W = 0.09a$. This result has been plotted in Fig. 2. In this figure, we can see that W/a increases approximately as $\psi_b^{1/2}$. This scaling could be expected because, for the vacuum field solution, the poloidal magnetic flux at the resonant surface scales linearly with ψ_b. At finite beta, resistive interchange modes become unstable; therefore, the effective width of the magnetic island increases. This scaling is also shown in Fig. 2, where the magnetic island width for $\beta/(2\varepsilon^2) = 0.0187$ has been plotted as a function of ψ_b.

For all cases considered, we follow the evolution of the plasma instabilities until their fluctuation level reaches a steady oscillatory solution (Fig. 3). At finite beta, the width of the magnetic island induced by the plasma instability oscillates in time as a result of the interaction between the resistive interchange instability, rotating at the diamagnetic velocity, and the vacuum magnetic field perturbation. The interaction between the resistive interchange instability and the vacuum magnetic field perturbation is quite complex. In Fig. 4, we have plotted the time evolution in the steady-state phase of the 5/8 magnetic island width for four different values of ψ_b. In the absence of vacuum magnetic field perturbation, $\psi_b = 0$, there is a poloidal rotation of the magnetic island induced by the plasma instability caused by a combination of E×B flows diamagnetic effects. The magnetic island associated with the instability rotates with a well-defined frequency. When a vacuum magnetic field perturbation is introduced, there is a braking effect that is most effective when both plasma and vacuum field perturbations are in phase and minimal when they are out of phase. Their interaction is suggestive of a stick-and-slip type of effect (Fig. 5). A similar braking effect has been observed in the case of tearing modes in tokamak plasmas.[11]

As ψ_b is increased, the oscillations of the magnetic island go through a period doubling. This is the case of $\psi_b = 5\times10^{-5}$, shown in Fig. 4. For a range of values of ψ_b, $1\times10^{-4} \le \psi_b < 2\times10^{-4}$, the evolution of the plasma instability has a chaotic behavior. In these cases, the stick-and-slip effect is more apparent. This effect can be seen in Fig. 5, where we have plotted the poloidal position, θ, of the O-point of the magnetic island as a function of time. Because we are considering an $m = 5$ perturbation, when θ reaches 72°, the poloidal

angle jumps back to zero and the island has rotated by 1/5 of the poloidal circumference. In Fig. 5, we see that the island oscillates for a while around $\theta = 0°$, and then suddenly the poloidal excursion increases and the island go through a full rotation.

Above a threshold value of the vacuum magnetic field perturbation, corresponding to a value ψ_{th} of the poloidal flux at the boundary, the poloidal propagation of the magnetic island in the plasma stops. The sticking effect becomes dominant, and the magnetic island acquires a quasi-periodic oscillation in the poloidal direction. The threshold value is difficult to determine from the numerical calculations. From the numerical results available, we can give bounds to the value of the threshold $1.75 \times 10^{-4} < \psi_{th} < 2.0 \times 10^{-4}$. This threshold not only is important in the dynamics of the fluctuations, but also plays an important role in the shear flow amplification.

IV. EFFECT OF THE VACUUM FIELD MAGNETIC ISLAND ON FLOW GENERATION

Let us now consider the effect of the vacuum magnetic island in the generation of a global poloidal flow through Reynolds stress. The non-diagonal $r\theta$ component of the Reynolds stress tensor has two terms, an electrostatic and a magnetic component, as it is shown in Eq. (13). For values of ψ_b below the threshold ψ_{th}, the electrostatic and magnetic components of the Reynolds stress have similar size and radial profile shape, but they have opposite sign (Fig. 6). This causes a near cancellation of these two terms, as happens often for electromagnetic turbulence.[12,13] In this regime, the electrostatic component is slightly larger than the magnetic. Therefore, there is weak poloidal flow amplification in the direction determined by the electrostatic term. For values of the vacuum magnetic field perturbation above the threshold, this perturbation induces a non-negligible contribution to the magnetic component of the Reynolds stress, making the latter dominant (Fig. 7). Therefore, for $\psi_b > \psi_{th}$, a strong sheared poloidal flow is established. This shear flow has the opposite sign from the one below the threshold.

The role of the vacuum magnetic field perturbation can be better clarified by splitting the magnetic field in two components, the instability induced and the vacuum magnetic field perturbations. In this case, the magnetic component of the Reynolds stress can be written as

$$\left\langle \tilde{B}_r \tilde{B}_\theta \right\rangle \equiv \left\langle \tilde{B}_r^p \tilde{B}_\theta^v + \tilde{B}_r^v \tilde{B}_\theta^p \right\rangle + \left\langle \tilde{B}_r^p \tilde{B}_\theta^p \right\rangle \quad . \tag{14}$$

Here, the superindex p refers to the instability-induced perturbation and v to the vacuum magnetic field perturbation. It is through the first term in the r.h.s. of Eq. (14) that the vacuum magnetic field perturbation contributes to the poloidal shear flow, by beating with the radially inhomogeneus component of the resistive interchange instability.

In Fig. 8, we have plotted the electrostatic and magnetic components of the Reynolds stress for the same case as in Fig. 7, but subtracting from the magnetic field perturbation the contribution of the vacuum magnetic field perturbation. We can see that the magnitude and radial profile of the Reynolds stress are similar to the ones below the threshold ψ_{th}. In Fig. 8, the two components of the Reynolds stress and the total are similar to the ones shown in Fig. 6.

Increasing the vacuum magnetic field perturbation increases the magnetic contribution to the Reynolds stress. This effect was not *a priori* obvious. Increasing the vacuum magnetic field perturbation increases the radial transport. The consequence could have been a reduction of the gradient drive of the resistive interchange and, therefore, a reduction of the overall contribution to the Reynolds stress. However, the numerical result is not that and the magnetic contribution to the Reynolds stress increases with ψ_b. When this magnetic contribution is large enough to cancel the electrostatic contribution, the result is the threshold effect and a reversal of the averaged poloidal sheared flow. When ψ_b is above the threshold, the averaged poloidal flow increases in direct proportion to the vacuum magnetic field contribution. In Fig. 9, we have plotted the averaged poloidal flow, $\overline{\langle V_\theta \rangle}$, for different values of the vacuum magnetic field perturbation showing the changes just described. Here, the angular brackets, $\langle\ \rangle$, indicate poloidal and toroidal angle averaged, and the over bar indicates time averaged. If an external coil induces the vacuum magnetic field perturbation, this coil can be used to control the local sheared flow.

The plots in Figs. 6–9 correspond to poloidal and toroidal angle averaged quantities, but they also have been averaged in time over the steady-state phase of the calculation. This second average eliminates the fast oscillations on each of these components. These oscillations can be

quite important. In Fig. 10, we have plotted the standard deviation (in time) of the average (in poloidal and toroidal angles) poloidal flow, $\left(\overline{\langle V_\theta \rangle^2 - \overline{\langle V_\theta \rangle}^2}\right)^{1/2}$. We can see that the oscillatory component of the averaged poloidal flow is more important below the threshold ψ_{th}. Above the threshold, where the averaged poloidal flow is large, the oscillatory component of the averaged poloidal is smaller than the stationary component.

V. SELF-ORGANIZATION: SHEARED FLOW AMPLIFICATION AND FLUCTUATION REDUCTION

In the present study, we consider a dynamical problem that involves a strong coupling between the fluctuations and shear flow. Fluctuations through Reynolds stress cause an amplification of shear flow, and the latter causes a reduction of the fluctuations. A nonlinear self-consistent solution emerges that couples both mechanisms. Since the problem involves a single helicity and there is no background turbulence, this problem involves a reorganization of the radial profiles of flow and fluctuations and it does not necessarily imply fluctuation suppression by shear flow. The radial profile of the perturbation rearranges itself to coexist with the shear flow and conversely. An interesting aspect of the present problem is that the vacuum magnetic field perturbation acts as an external knob that allows us to vary this solution and test the nature of this self-organization process.

For $\psi_b < \psi_{th}$, the oscillatory component of the fluctuations and flow are dominant over the stationary ones, as we discussed in the previous section. For $\psi_b > \psi_{th}$ and for both flow and fluctuation level, the steady-state component is the largest component of the solution. However, the oscillatory component is still significant. To show the essentially dynamical character of the coupling of fluctuations and flows, we have plotted the value of the density fluctuations at $r/a = 0.7$, near the inner peak of its rms value, as a function of the shear flow at the singular surface. In Fig. 11, we show this plot for a case without vacuum field perturbation $(\psi_b = 0)$ and for one case with ψ_b above the threshold $(\psi_b = 2\times 10^{-4})$.

A main question is what is the guiding principle of the profile reorganization process. To explore this issue, we have calculated the shearing rate for the sequence of nonlinear calculations with different values of ψ_b. Since the local shear flow varies in time and position in a rather sensitive manner, we have defined an averaged valued for the shear flow in the following way:

$$\{V_\theta'\} = \left\{ 2\int_0^a r dr \langle V_\theta'(r)\rangle^2 \right\}^{1/2} \tag{15}$$

We define the shearing rate as $\omega_s = \{V_\theta'\} k_\theta W$ and the normalized shearing as $\Omega_s = \omega_s/\gamma_0$. Here, $k_\theta = 5/r_s$ and $W = 0.06a$, and γ_0 is the linear growth rate of the 5/8 instability. We have calculated γ_0 using the density and temperature profiles reached in the steady state with the vacuum island and without flow. The calculated Ω for the sequence considered is shown in Fig. 12. For values of ψ_b below the threshold, the level of shear flow generated and the change in the gradient of the profile are such that $\Omega \approx 1$. For values of ψ_b above the threshold, $\Omega > 1$. It appears like that below the threshold the fluctuations and flows organize themselves so as to be close to marginal stability. It is important to use the rms value of V_θ' in the calculation of the shearing rate to take into account the oscillatory component of the flow.

We cannot expect that the radially integrated stability criterion describes all details of the self-organization process. The poloidal flow oscillates in time and changes direction in a quasiperiodic manner. The averaged poloidal flow has radial spikes just outside the magnetic island, and the maximum shear is at the resonant surface (Fig. 9). The corresponding fluctuations have a minimum at the resonant surface, and they peak away from the resonant

surface where the flow has the minimum shear. In Fig. 13, the rms value of the density fluctuation is plotted as a function of radius. The profiles are obtained by averaging in time in two different time intervals in the saturation phase. For $\psi_b < \psi_{th}$, the fluctuation level and flow profiles do not change much with ψ_b, and the integrated criterion is reliable. However, for $\psi_b > \psi_{th}$, there is a radial rearrangement of the profiles as ψ_b increases. The fluctuation levels are very low in the region of high shear flow; conversely, in the region of high fluctuations, there is hardly any flow. Furthermore, although the oscillatory component of the flow has decreased, it is still quite significant. In this situation, we need a local criterion to describe the self-organization. The integrated one is no longer reliable.

The saturation level of the fluctuations is only slightly decreased for island widths below the threshold; and, in spite of the strong sheared flow, the fluctuation level increases for island widths above the threshold, as is shown in Fig. 13. However, the fluctuation-induced particle flux [Eq. (10)] in this region, $\psi_b > \psi_{th}$, remains almost the same as the vacuum magnetic field perturbation increases, as can be seen in Fig. 14.

The total particle flux is essentially given by the electrostatic component. The effect of the magnetic field perturbation in Eq. (10) is practically negligible in the range of parameters considered here. That is not the situation for the energy flux. There is a non-negligible contribution from the magnetic field perturbation, as can be seen in Fig. 15. This magnetic contribution increases with increasing vacuum magnetic field perturbation. However, the total heat flux is not much affected (Fig. 16). There is a reduction of the electrostatic flux by the shear flow. This reduction practically compensates for the increase of the magnetic component.

Therefore, the profile reorganization process is such that the instability is kept close to marginal, and both particle and heat flux remain constant as the vacuum magnetic field perturbation is varied.

VI. CALCULATION OF AVERAGES IN THE PRESENCE OF A VACUUM MAGNETIC ISLAND

When there are static perturbations in the plasma, as is the case for a vacuum magnetic island in a stellarator, there is a problem in using a time average instead of a flux surface average and/or ensemble average. Since experimentalists often measure fluctuations only in a single poloidal position, a time average is often used instead of flux surface average. In this case, the presence of a stationary perturbation can cause serious distortions of the results. We can use the results of the numerical calculations presented in this paper to illustrate some of these difficulties. Let us consider the fluctuation-induced electrostatic particle flux. We use the following form to calculate the flux from the numerical results:

$$\Gamma_{\text{model}} = \overline{\left\langle \left(V_r - \langle V_r \rangle\right)\left(n - \langle n \rangle\right) \right\rangle} \quad , \tag{16}$$

where the upper bar indicates time-average and the angular brackets, $\langle\ \rangle$, indicate average over the flux surface. In the experiment, with data measured at a single poloidal location, the averaged flux is often calculated as

$$\Gamma_{\text{exp}} = \overline{\left(V_r - \overline{V}_r\right)\left(n - \overline{n}\right)} \quad . \tag{17}$$

In the absence of a vacuum magnetic island and with poloidal propagation of the turbulence, both results are similar. This can be seen in Fig. 17, where we have plotted the particle flux calculated by Eq. (17) with data taken at a single poloidal position and the particle flux calculated by Eq. (16). The comparison is done for several values of the poloidal angle and using the numerical data for the $\psi_b = 0$ case. The results show good agreement between the two methods. The situation changes totally when poloidal propagation of some or all fluctuation components stops. In Fig. 18, we present a plot analogous to Fig. 17 but for the $\psi_b = 2\times10^{-4}$ case. It is clear from Fig. 18 that Eq. (17) underestimates the flux in practically all poloidal positions, and even may result in a strong negative flux in some of them, because the estimates of the averaged fluctuation level are erroneous and close to its local value.

Recent experiments carried out in the TJ-II stellarator have shown that local E×B fluctuation induced fluxes are significantly modified in the proximity of rational surfaces. In the case of measurements taken in the proximity of the $n = 4/m = 2$ resonant surface, located

near the plasma boundary, the local E×B fluctuation particle flux shows a reverse direction (from outwards to inwards). Further measurements of E×B turbulent transport are in progress at different poloidal and toroidal locations in the TJ-II stellarator to clarify to what extend this is a local or a global effect linked to rational surfaces.

VII. CONCLUSIONS

Experiments in the TJ-II stellarator show the formation of E×B sheared flows in the proximity of rational surfaces. These results can be interpreted in terms of the symmetry-breaking mechanisms in the radial-poloidal structure of fluctuations (i.e., Reynolds stress) at rational surfaces. We have used a resistive interchange model to study the effect of magnetic islands on poloidal flow generation and turbulence. For vacuum magnetic islands below a threshold value, there is a near cancellation of the electrostatic and magnetic components of the Reynolds stress. Above the threshold, the magnetic component dominates and a strong sheared flow is established. In spite of that, the fluctuation level increases, and the particle and the heat flux remain almost the same.

Similar results were obtained in the study of resistive pressure-gradient-driven turbulence with an external sheared flow.[11] In that case, the numerical results showed that shear flow effects were not significant when the single helicity dominated near the low-m rational surfaces. Therefore, multiple helicity calculations are needed to assess the effect of vacuum islands on turbulence. These calculations are now under way.

Care should be taken in evaluating the turbulent flux in stellarators. The presence of small vacuum magnetic field islands can stop the poloidal propagation of some of the fluctuation components. Under these circumstances, the flux surface average and time average are not equivalent. The result may be an erroneous estimation of the averaged value of the fluctuations and, as a consequence, an erroneous estimation of the fluxes.

Acknowledgments

This research is sponsored by the Dirección General de Investigación (Spain) under Project No. FTN2000-0924-C03. Part of this research has been carried out at Oak Ridge

National Laboratory, managed by UT-Battelle, LLC, for the U.S. Department of Energy under contract number DE-AC05-00OR22725.

References

[1]K. H. Burrell, *Phys. Plasmas* **4**, 1499 (1997).

[2]P. W. Terry, *Rev. Modern Phys*. **72**, 109 (2000).

[3]E. Synakowski, *Plasma Phys. Control. Fusion* **40**, 581 (1998).

[4]Y. Koide, M. Kikuchi, M. Mori *et al*., *Phys. Rev. Lett.* **72**, 3662 (1993).

[5]K. Ohyabu K. Noorihara, M. Funaba, *Phys. Rev. Lett*. **84**, 103 (2000).

[6]G. Grieger, WVII Team, NI Team, ECRH Group, Plasma Phys. Controlled Fusion **28**, 1A, 43 (1986)

[7]M. A. Pedrosa, C. Hidalgo, A. Lopez-Fraguas, *et al.*, *Czechoslovak Journal of Physics* **50**, 1463 (2000).

[8]C. Hidalgo, M. A. Pedrosa, E. Sanchez, *Plasma Phys. Control. Fusion* **42**, A153 (2000).

[9]C. Alejaldre, J. Alonso, L. Almoguera, *Plasma Phys. Control. Fusion* **41**, B109 (1999).

[10]J. M. Greene and J. L. Johnson, *Phys. Fluids* **4**, 875 (1961).

[11]R. J. LaHaye, C. L. Retting, R. J. Groebner, A. W. Hyatt, and J. T. Seville, *Phys. Plasmas* **1**, 373 (1996).

[12]G. G. Craddock and P. H. Diamond, *Phys. Rev. Lett.* **67**, 1535 (1991).

[13]B. A. Carreras, V. E. Lynch, L. Garcia, P. H. Diamond, *Phys. Fluids* B **5**, 1491 (1993).

Figure captions

Fig. 1. Electron density and temperature profiles, normalized to their peak value, and rotational transform profile used in these calculations.

Fig. 2. Magnetic island width of the 5/8 helicity as a function of the boundary value of the poloidal flux for a vacuum magnetic field and for a case with finite beta.

Fig. 3. Time evolution of the rms of the poloidal magnetic flux and velocity stream function showing that they reach to a steady-state phase.

Fig. 4. Time evolution of the 5/8 magnetic island width for four values of ψ_b. The time period is during the steady-state phase of the calculation. The vertical scale has been arbitrarily shifted for the purpose of the drawing.

Fig. 5. Poloidal position of the O-point of the magnetic island plotted as a function of time. The position is measured by the poloidal angle θ in degrees. The time period corresponds to the steady-state phase of the evolution for $\psi_b = 1.5\times10^{-4}$.

Fig. 6. Radial profiles of the Reynolds stress and its components for $\psi_b = 5\times10^{-5}$. They are obtained by time-averaging in the saturation phase.

Fig. 7. Radial profiles of the Reynolds stress and its components for $\psi_b = 2\times10^{-4}$. They are obtained by time averaging in the saturation phase.

Fig. 8. Radial profiles of the Reynolds stress and its components for $\psi_b = 2\times10^{-4}$ after subtracting the components of the vacuum magnetic field perturbation. They are obtained by time averaging in the saturation phase.

Fig. 9. Radial profiles of the averaged poloidal flow for different values of ψ_b. They are obtained by time averaging over the saturation phase of the calculation.

Fig. 10. Radial profiles of the standard deviation (in time) of the averaged poloidal flow for different values of ψ_b. They are obtained over the saturation phase of the calculation.

Fig. 11. Value of the density fluctuation level at $r/a = 0.7$ as a function of the shear flow at the singular surface for a case without vacuum field perturbation $(\psi_b = 0)$ and one case with ψ_b above the threshold $(\psi_b = 2\times10^{-4})$.

Fig. 12. Normalized shearing rate as a function of ψ_b.

Fig. 13. Radial profiles of the rms values of the density fluctuations for different sizes of the vacuum magnetic island. They are obtained by averaging in the saturation phase.

Fig. 14. Radial profiles of the rms values of the turbulence-induced electrostatic particle fluxes for different sizes of the vacuum magnetic island. They are obtained by averaging in the saturation phase.

Fig. 15. Radial profiles of the rms values of the turbulence-induced electrostatic components of the heat flux compared with the total heat flux for the $\psi_b = 2\times10^{-4}$ case.

Fig. 16. Radial profiles of the rms values of the turbulence-induced heat fluxes for different sizes of the vacuum magnetic island. They are obtained by averaging in the saturation phase.

Fig. 17. Particle flux calculated by Eq. (17) with data taken at a single poloidal position (thin lines) and the particle flux calculated by Eq. (16) (thick line). The comparison is done for several values of the poloidal angle and using the numerical data for the $\psi_b = 0$ case.

Fig. 18. The same plot as in Fig. 17, but for the $\psi_b = 2\times10^{-4}$ case.

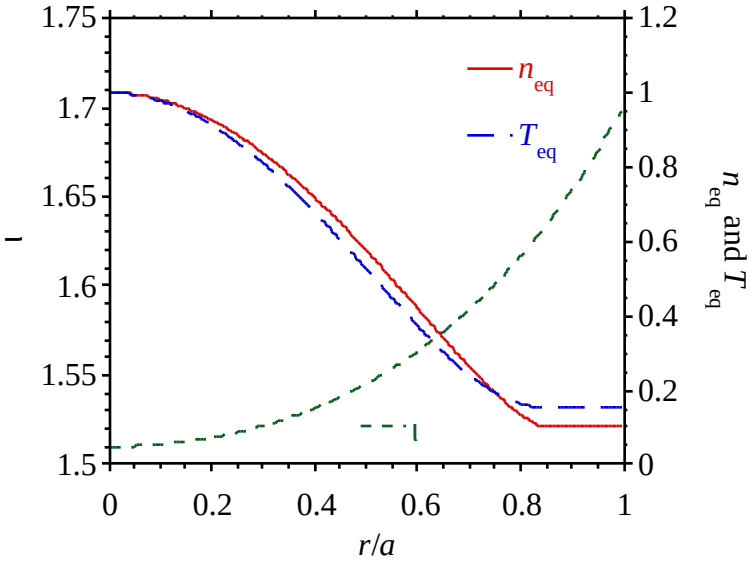
1.75
1.7
1.65
1.6
1.55
1.5
ι
1.2
1
0.8
0.6
0.4
0.2
0
n_{eq} and T_{eq}
n_{eq}
T_{eq}
ι
0
0.2
0.4
0.6
0.8
1
r/a

Fig. 1

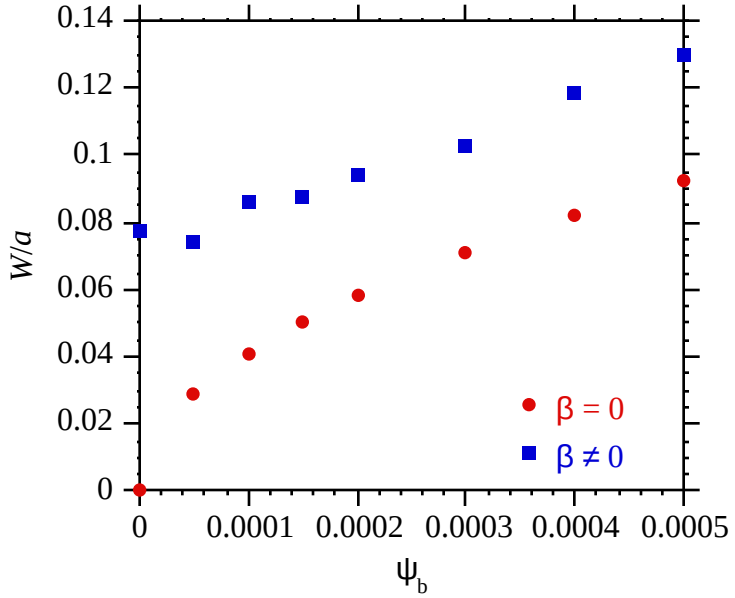
0.14
0.12
0.1
0.08
0.06
0.04
0.02
0
W/a
β = 0
β ≠ 0
0
0.0001
0.0002
0.0003
0.0004
0.0005
ψ_b

Fig. 2

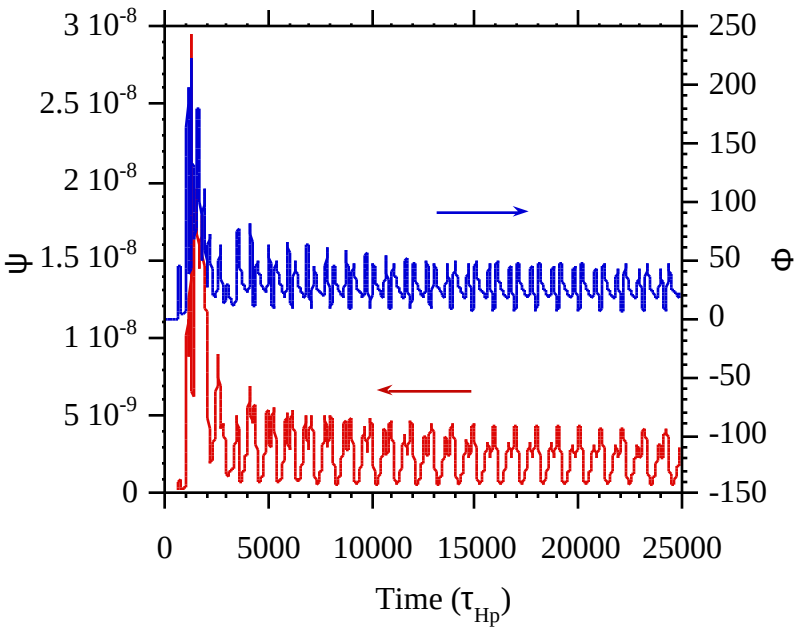
3 10-8
2.5 10-8
2 10-8
1.5 10-8
1 10-8
5 10-9
0
Ψ
250
200
150
100
50
0
-50
-100
-150
Θ
0
5000
10000
15000
20000
25000
Time (τHp)

Fig. 3

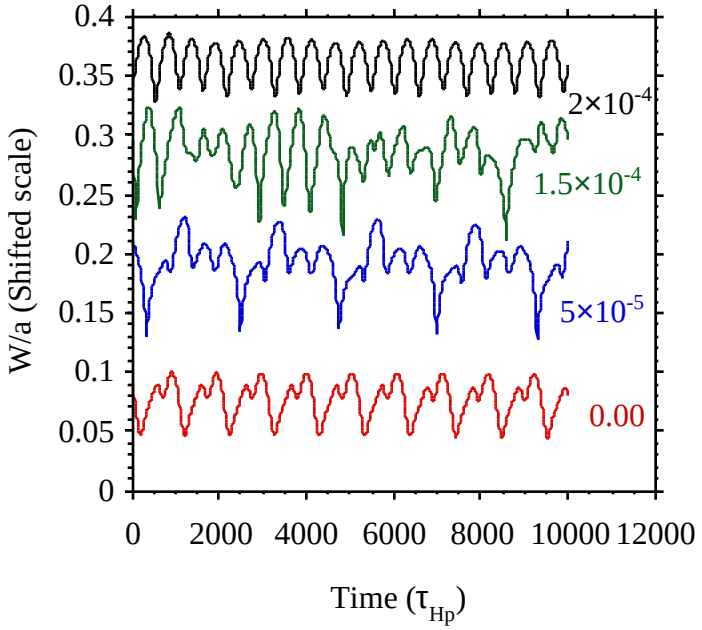
0.4
0.35
0.3
0.25
0.2
0.15
0.1
0.05
0
W/a (Shifted scale)
2×10-4
1.5×10-4
5×10-5
0.00
0
2000
4000
6000
8000
10000
12000
Time (τHp)

Fig. 4

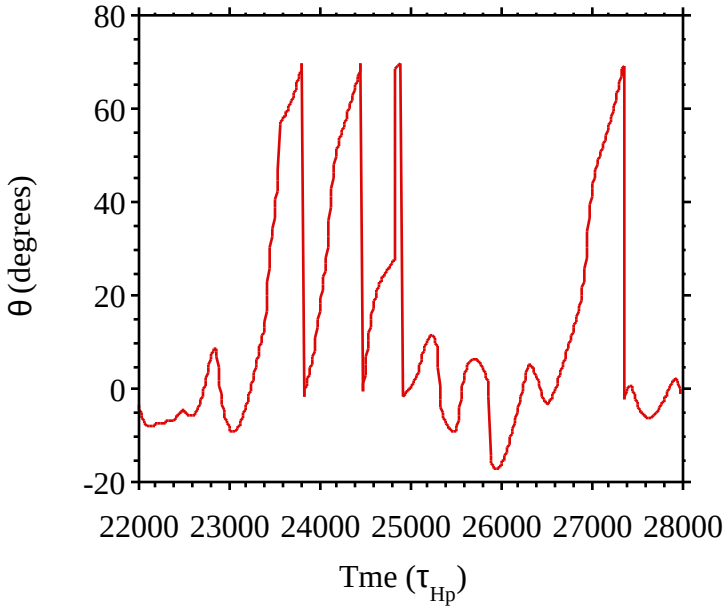
80
60
40
20
0
-20
θ (degrees)
22000 23000 24000 25000 26000 27000 28000
Tme (τ_{Hp})

Fig. 5

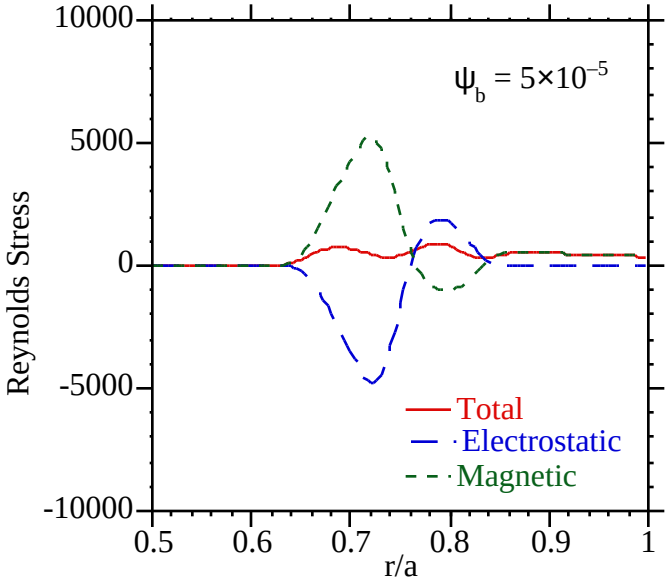
10000
5000
0
-5000
-10000
Reynolds Stress
$\psi_b = 5\times10^{-5}$
Total
Electrostatic
Magnetic
0.5 0.6 0.7 0.8 0.9 1
r/a

Fig. 6

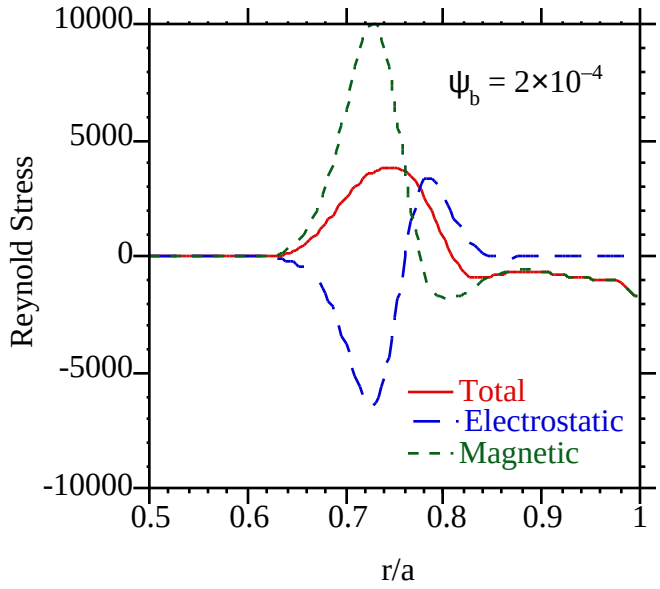
10000
5000
0
-5000
-10000
Reynold Stress
$\psi_b = 2\times10^{-4}$
Total
Electrostatic
Magnetic
0.5
0.6
0.7
0.8
0.9
1
r/a

Fig. 7

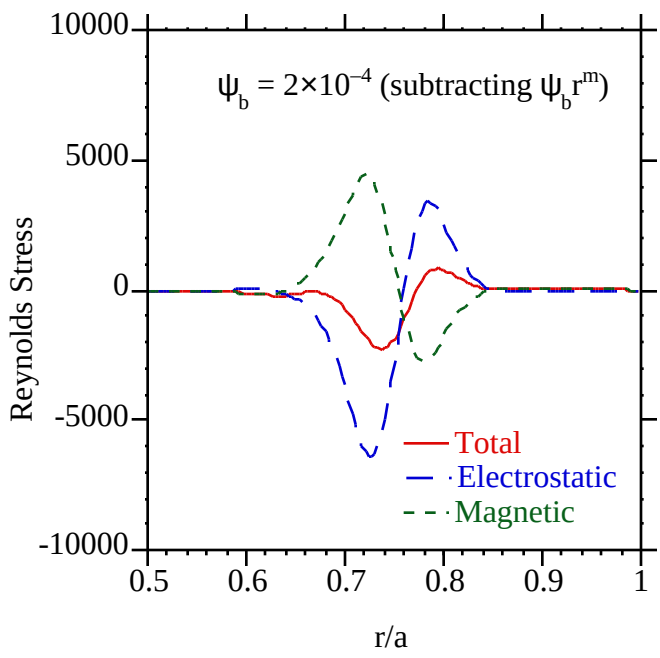
10000
5000
0
-5000
-10000
Reynolds Stress
$\psi_b = 2\times10^{-4}$ (subtracting $\psi_b r^m$)
Total
Electrostatic
Magnetic
0.5
0.6
0.7
0.8
0.9
1
r/a

Fig. 8

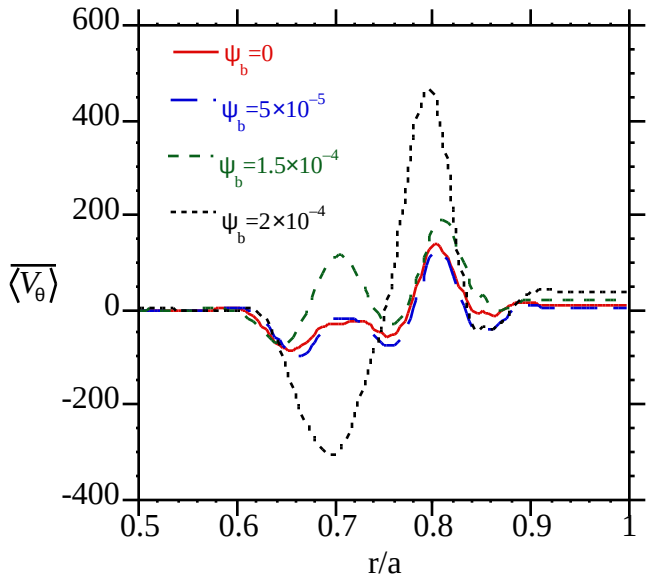
600
400
200
0
-200
-400
0.5
0.6
0.7
0.8
0.9
1
r/a
$\overline{\langle V_\theta \rangle}$
ψ_b=0
ψ_b=5×10^{-5}
ψ_b=1.5×10^{-4}
ψ_b=2×10^{-4}

Fig. 9

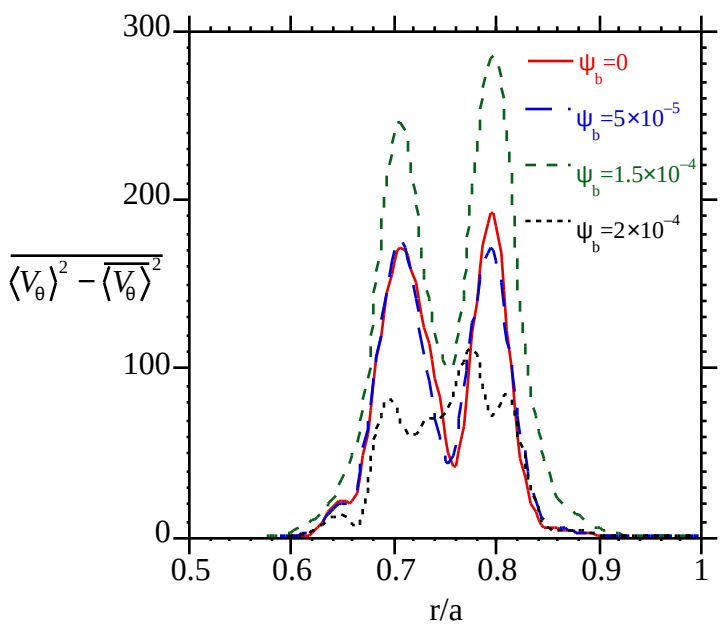
300
200
100
0
0.5
0.6
0.7
0.8
0.9
1
r/a
$\overline{\langle V_\theta \rangle^2 - \overline{\langle V_\theta \rangle}^2}$
ψ_b=0
ψ_b=5×10^{-5}
ψ_b=1.5×10^{-4}
ψ_b=2×10^{-4}

Fig. 10

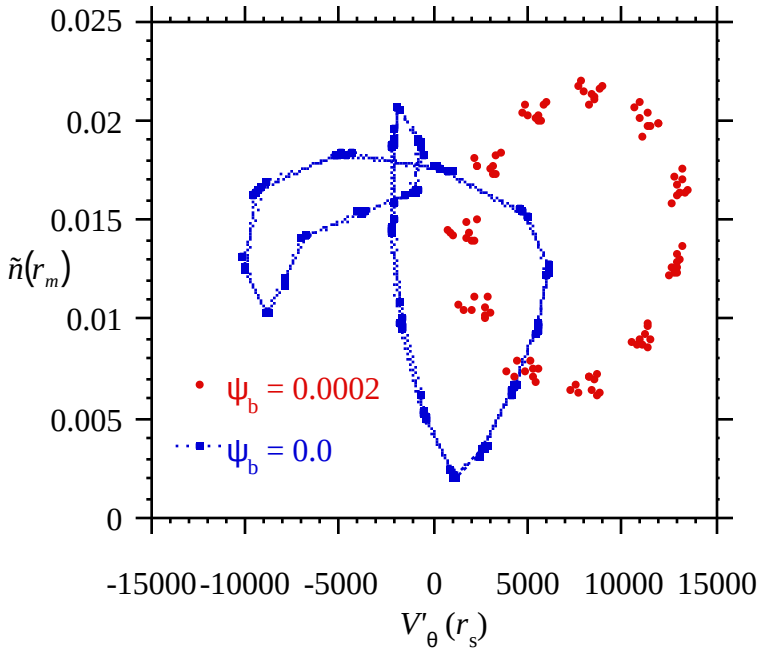
0.025
0.02
0.015
0.01
0.005
0
$\tilde{n}(r_m)$
ψ_b = 0.0002
ψ_b = 0.0
-15000 -10000 -5000 0 5000 10000 15000
$V'_\theta(r_s)$

Fig. 11

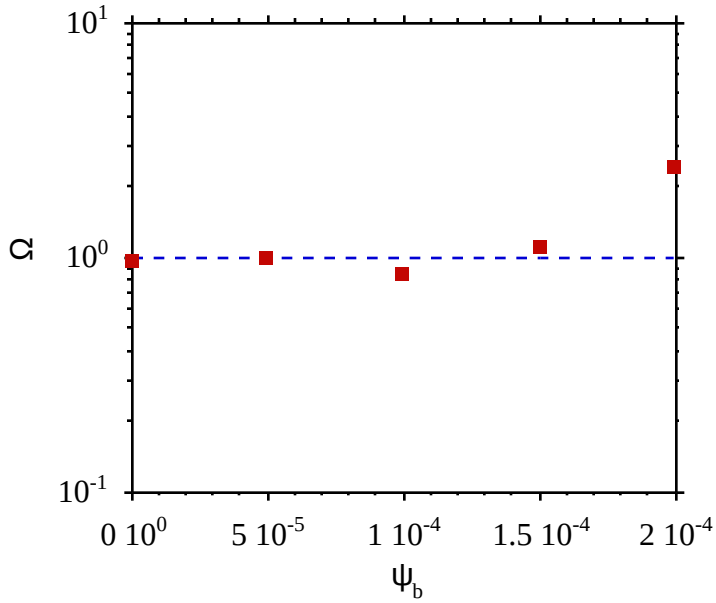
10^1
10^0
10^{-1}
Ω
0 10^0
5 10^{-5}
1 10^{-4}
1.5 10^{-4}
2 10^{-4}
ψ_b

Fig. 12

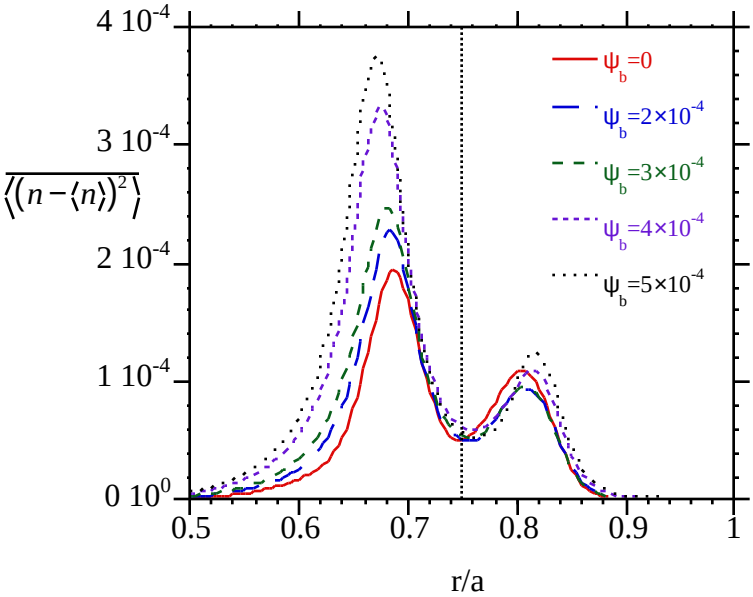
4 10-4
3 10-4
2 10-4
1 10-4
0 100
0.5
0.6
0.7
0.8
0.9
1
r/a
ψb=0
ψb=2×10-4
ψb=3×10-4
ψb=4×10-4
ψb=5×10-4

Fig. 13

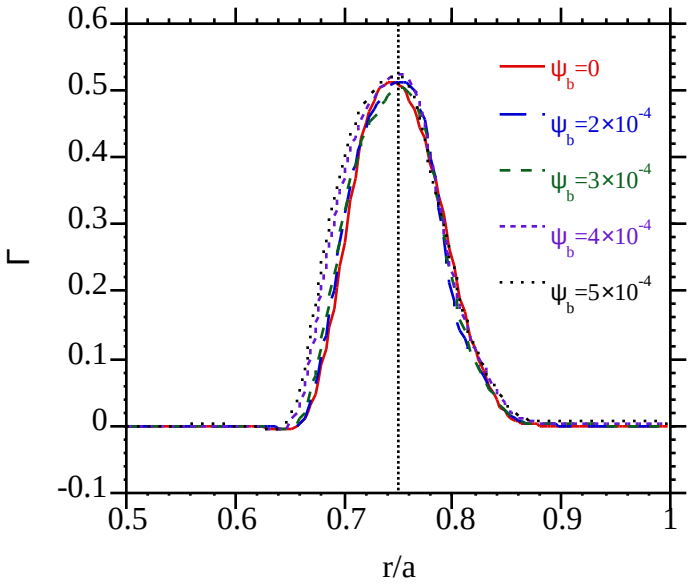
0.6
0.5
0.4
0.3
0.2
0.1
0
-0.1
Γ
0.5
0.6
0.7
0.8
0.9
1
r/a
ψb=0
ψb=2×10-4
ψb=3×10-4
ψb=4×10-4
ψb=5×10-4

Fig. 14

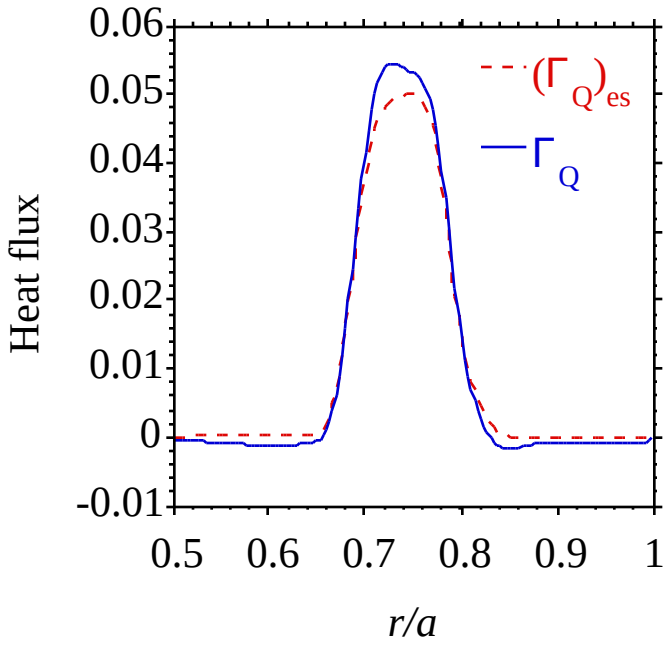
0.06
0.05
0.04
0.03
0.02
0.01
0
-0.01
Heat flux
0.5
0.6
0.7
0.8
0.9
1
r/a
(Γ_Q)_es
Γ_Q

Fig. 15

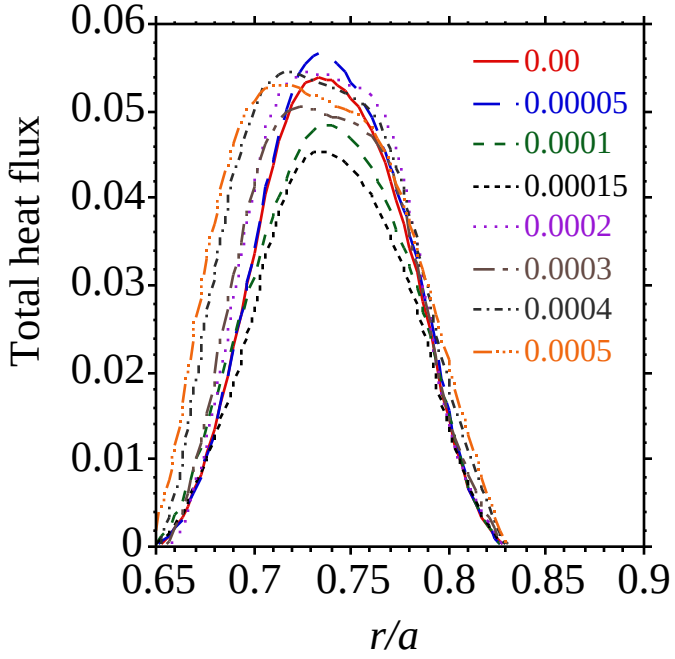
0.06
0.05
0.04
0.03
0.02
0.01
0
Total heat flux
0.65
0.7
0.75
0.8
0.85
0.9
r/a
0.00
0.00005
0.0001
0.00015
0.0002
0.0003
0.0004
0.0005

Fig. 16

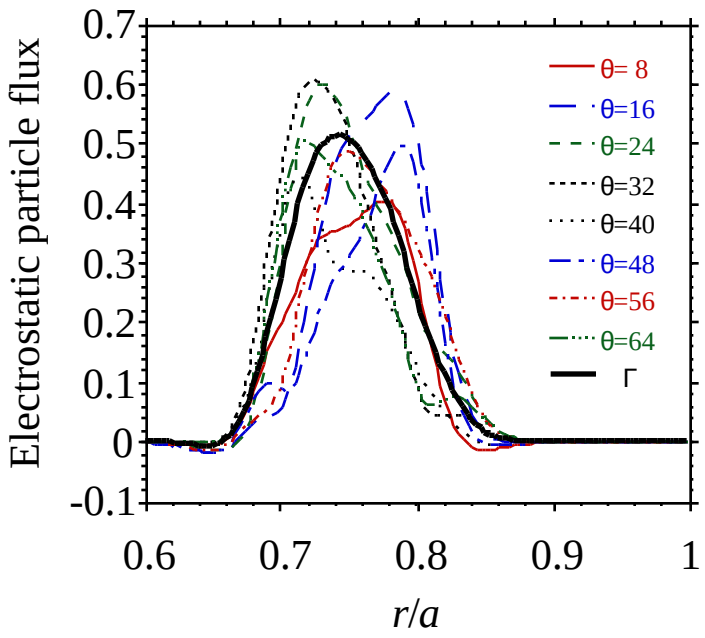
Electrostatic particle flux
0.7
0.6
0.5
0.4
0.3
0.2
0.1
0
-0.1
0.6
0.7
0.8
0.9
1
r/a
θ= 8
θ=16
θ=24
θ=32
θ=40
θ=48
θ=56
θ=64
Γ

Fig. 17

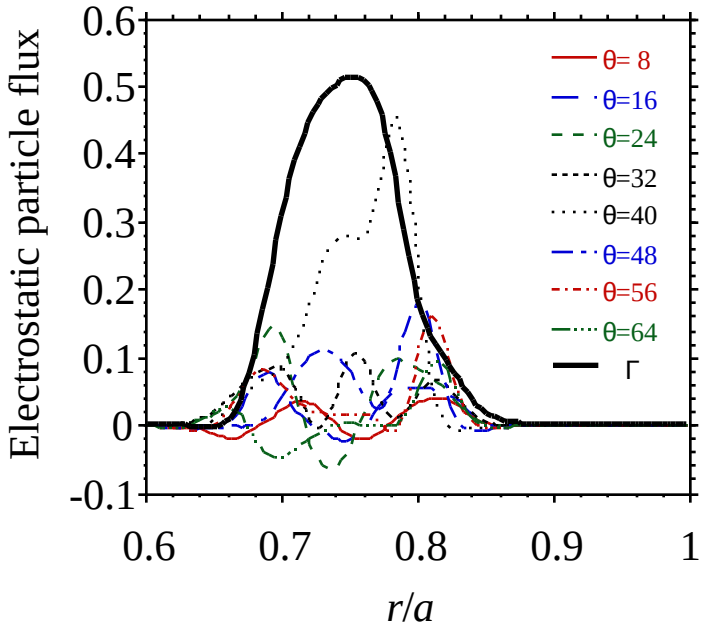
Electrostatic particle flux
0.6
0.5
0.4
0.3
0.2
0.1
0
-0.1
0.6
0.7
0.8
0.9
1
r/a
θ= 8
θ=16
θ=24
θ=32
θ=40
θ=48
θ=56
θ=64
Γ

Fig.18